SCIENCE CHINA
Physics, Mechanics & Astronomy

• Article •

August 2026 Vol. 69 No. 8: 284711
https://doi.org/10.1007/s11433-026-2992-9

Quaternionic lifting of spherical Clebsch maps in helical flows

Yanru Wang[1], Lei Pang[2], Zhenkun Li[3], Yukun Yan[1], Linlin Kang[4], Qinghai Zhang[2], and Shiying Xiong[1,5*]

[1]*Department of Engineering Mechanics, School of Aeronautics and Astronautics, Zhejiang University, Hangzhou 310027, China*
[2]*Institute of Fundamental and Transdisciplinary Research, School of Mathematical Sciences, Zhejiang University, Hangzhou 310058, China*
[3]*Academy of Mathematics and Systems Science, Chinese Academy of Sciences, Beijing 100190, China*
[4]*Hangzhou International Innovation Institute, Beihang University, Hangzhou 311115, China*
[5]*National Key Laboratory of Aerospace Physics in Fluids, Mianyang 621000, China*

Received February 24, 2026; accepted April 30, 2026; published online June 23, 2026

Vortices, or swirling flows, are fundamental features in many physical systems, ranging from ocean currents and weather patterns to superfluids and plasmas. However, accurately modeling these flows, particularly those with complex topological structures, has remained a significant challenge. This study introduces a mathematical framework for capturing the dynamics of vortex flows via a non-trivial lifting process from spherical vorticity maps to spherical velocity maps, enabling the velocity field to be expressed as a quaternion-valued wave function representing vortex tubes of arbitrary topology. The framework has broad applications across diverse fields, including turbulence, fluid dynamics, superfluid vortices, ocean circulation, and plasma physics, offering valuable insights into the topological evolution and stability of vortex structures in both natural and engineered systems.

fluid mechanics, helicity, vortex dynamics

Citation: Y. Wang, L. Pang, Z. Li, Y. Yan, L. Kang, Q. Zhang, and S. Xiong, Quaternionic lifting of spherical Clebsch maps in helical flows, Sci. China-Phys. Mech. Astron. **69**, 284711 (2026), https://doi.org/10.1007/s11433-026-2992-9

1 Introduction

The Aharonov-Bohm effect established electromagnetic potentials as physical entities that directly influence quantum phases and serve as fundamental gauge fields in quantum field theory, rather than mere mathematical conveniences of classical electromagnetism [1-3]. In a conceptually mirrored manner, spherical Clebsch maps, introduced by Chern et al. [4] following Kuznetsov and Mikhailov [5], generalize the traditional Clebsch representation to velocity and vorticity fields with nonzero helicity. In this framework, the vorticity field is represented by a spin via the Hopf fibration [6], capturing reduced fluid dynamics, while the velocity field, expressed as a quaternion-valued wave function, embodies the Hamiltonian formulation with intrinsic geometric character and gauge freedom [7]. The direct construction of velocity Clebsch maps with arbitrary topology remains challenging, motivating a lifting procedure from vorticity Clebsch maps to velocity Clebsch maps. Such a process transforms a reduced, vorticity-focused representation into a complete description of the fluid's full geometric and topological structure.

In this study, we introduce a comprehensive mathematical framework for quaternionic lifting of spherical Clebsch maps (QLSCM) within the Hopf fibration field [8], analytically resolving the solution uniqueness problem using classical formulations. This framework not only includes the projection of spherical velocity Clebsch maps onto spherical vorticity Clebsch maps, but also addresses the reverse pro-

*Corresponding author (email: shiying.xiong@zju.edu.cn)

cess of lifting spherical vorticity Clebsch maps to spherical velocity Clebsch maps, which forms the core contribution of our work.

We further develop a method to compute the corresponding spherical velocity Clebsch map from a given spherical vorticity Clebsch map. The latter is constructed using a method based on tubular structures of arbitrary shape and thickness, derived from explicit analytical expressions in a curved cylindrical coordinate system [9-11]. Through this lifting procedure, we achieve unique spherical velocity Clebsch maps associated with knotted flux tubes of arbitrary topology, including cases with varying thickness and uniform twist [12-15].

The QLSCM bridges gauge theory [16, 17], fiber-bundle geometry [18], and computational techniques [19-22], offering powerful tools for analyzing coherent structures with the quaternion-valued wave function embedding the velocity field's geometric and topological features to capture the full dynamics in fluids [23-25], describing the coupling between multiple superfluid components in plasmas [26, 27], and encoding both position and spin information to enable subsequent quantum operations such as measurement or Hamiltonian evolution in quantum systems [28-30].

The paper is structured as follows: sect. 2 introduces the mathematical framework based on the quaternionic kinematic ansatz, defining the mapping between quaternion-valued wave functions and spin fields, and establishing the correspondence between spherical velocity and vorticity Clebsch maps. Sect. 3 presents the theoretical derivations to construct unique solutions for the spherical velocity Clebsch maps from the spherical vorticity Clebsch maps, and achieve precise velocity-vorticity matching via functional optimization. Sect. 4 applies QLSCM to construct knotted vortex tubes by obtaining spherical vorticity Clebsch maps through analytical solutions and spherical velocity Clebsch maps via numerical algorithms. Subsequently, it analyzes their geometric and topological properties, investigates their dynamic evolution in incompressible Schrödinger flows (ISFs). Sect. 5 summarizes the key findings of the QLSCM framework and discusses its broad implications for future research, ranging from turbulence modeling to quantum algorithms in fluid dynamics.

2 Quaternionic kinematic ansatz

We represent incompressible flow using a normalized quaternionic wave function, whose adjoint action produces a unit spin on the 2-sphere. This spin captures the vortex geometry as a sphere-valued texture, while the wave function induces a divergence-free velocity field through a spherical Clebsch map. It aligns with the idea in refs. [31-34] that uses three independent variables to capture the full geometric and topological structure of the flow. From an algebraic perspective, the quaternions employed in this study are isomorphic to the $SU(2)$ representation generated by Pauli matrices. Consequently, the proposed framework can be reformulated using the two-dimensional Pauli matrix representation.

In the QLSCM framework, ψ serves as an auxiliary field that facilitates the construction of two distinct physical quantities, the velocity field $\boldsymbol{u}_\psi$ representing the fundamental field in classical fluid mechanics, and the spin field $\boldsymbol{\varsigma}$ characterizing the topological structure of the flow. Dynamically, ψ provides a gauge-invariant representation that unifies the mathematical description of diverse fluid systems, including inviscid flows, viscous flows, and ISFs.

2.1 Spherical Clebsch map

We consider a quaternion-valued wave function $\psi : \Omega \subset \mathbb{R}^3 \to \mathbb{H}$,

$$\psi = a + b\,\mathrm{i} + c\,\mathrm{j} + d\,\mathrm{k}, \tag{1}$$

with real components a, b, c, d and quaternionic units $\mathrm{i}, \mathrm{j}, \mathrm{k}$. The isomorphism $\boldsymbol{I}_{\mathrm{iso}} : \mathbb{H} \to \mathbb{R}^4$ maps $a + b\,\mathrm{i} + c\,\mathrm{j} + d\,\mathrm{k}$ to (a, b, c, d) [35], giving $\boldsymbol{\psi} := \boldsymbol{I}_{\mathrm{iso}} \circ \psi$. The normalization

$$|\psi|^2 = a^2 + b^2 + c^2 + d^2 = 1 \tag{2}$$

restricts ψ to $\mathbb{H}_{\mathbb{S}^3}$. The spin is defined by the adjoint action

$$\varsigma := \overline{\psi}\ \mathrm{i}\ \psi, \tag{3}$$

which is a purely imaginary unit quaternion, satisfying

$$\mathrm{Re}(\varsigma) = 0, \quad |\varsigma|^2 = 1. \tag{4}$$

The three imaginary components of ς are given by

$$\varsigma_1 = a^2 + b^2 - c^2 - d^2, \quad \varsigma_2 = 2(bc - ad), \quad \varsigma_3 = 2(ac + bd). \tag{5}$$

ς realizes the Hopf fibration $\pi : \mathbb{H}_{\mathbb{S}^3} \to \mathbb{H}_{\mathbb{S}^2}$, $x \mapsto \overline{x}\,\mathrm{i}\,x$ [6]. Composing with $\boldsymbol{I}_{\mathrm{iso}}$ gives $\boldsymbol{\varsigma} := \boldsymbol{I}_{\mathrm{iso}}|_{\mathbb{H}_{\mathbb{S}^2}} \circ \varsigma \in \mathbb{S}^2$ and the induced map $\tilde{\pi} : \mathbb{S}^3 \to \mathbb{S}^2$ with $\boldsymbol{\varsigma} = \tilde{\pi} \circ \boldsymbol{\psi}$.

The definition of the spin field $\boldsymbol{\varsigma}$ in eq. (3) differs from its representation in standard quantum mechanics. In the quantum context, the spin vector is typically constructed using the Pauli spinor and the three Pauli matrices symmetrically. In contrast, the current definition employs only the imaginary unit i, breaking the algebraic symmetry among the quaternionic units i, j, and k. Geometrically, this symmetry breaking identifies a specific fiber direction for the Hopf fibration, projecting the 3-sphere onto the 2-sphere. Figure 1 summarizes these correspondences among Ω, $\mathbb{H}_{\mathbb{S}^3}$, $\mathbb{H}_{\mathbb{S}^2}$, $\mathbb{S}^3$, and $\mathbb{S}^2$. See Supplementary Note 1A for more details.

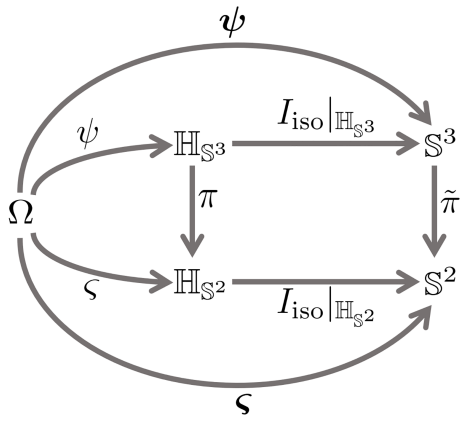

Figure 1 Quaternionic Hopf setup. A unit-quaternion map $\psi : \Omega \to \mathbb{H}_{\mathbb{S}^3}$ induces $\boldsymbol{\varsigma} = \overline{\psi}\,\mathrm{i}\,\psi \in \mathbb{H}_{\mathbb{S}^2}$. Under $\mathbb{H} \simeq \mathbb{R}^4$ these give $\boldsymbol{\psi} \in \mathbb{S}^3$, $\boldsymbol{\varsigma} \in \mathbb{S}^2$, with projections π and $\tilde{\pi}$.

Within this structure, the velocity admits the spherical Clebsch form [4,5,19]

$$\boldsymbol{u}_\psi := \hbar\ \mathrm{Re}\ (\boldsymbol{\nabla}\overline{\psi}\ \mathrm{i}\ \psi), \tag{6}$$

with the constant $\hbar$ associated with the velocity circulation and incompressibility $\boldsymbol{\nabla}\cdot\boldsymbol{u}_\psi = 0$ with the Coulomb gauge is equivalent to

$$\mathrm{Re}\ (\nabla^2\overline{\psi}\ \mathrm{i}\ \psi) = 0. \tag{7}$$

Writing $\boldsymbol{\varsigma} = \varsigma_1\,\mathrm{i} + \varsigma_2\,\mathrm{j} + \varsigma_3\,\mathrm{k}$, the vorticity Clebsch map takes the symmetric form

$$\boldsymbol{\omega}_\varsigma := \frac{\hbar}{4}\varepsilon_{abc}\,\varsigma_a\,\boldsymbol{\nabla}\varsigma_b \times \boldsymbol{\nabla}\varsigma_c, \tag{8}$$

where ε_{abc} is the Levi-Civita symbol, and under standard smoothness conditions, it corresponds to the curl of $\boldsymbol{u}_\psi$,

$$\boldsymbol{\omega}_\varsigma = \boldsymbol{\omega}_\psi := \boldsymbol{\nabla} \times \boldsymbol{u}_\psi. \tag{9}$$

Mathematically, the $\boldsymbol{\varsigma}$ field maps to the 2-sphere $\mathbb{S}^2$, which relates to the construction of the topological degree of the Hopf map. Specifically, $\boldsymbol{\omega}_\varsigma$ defined in eq. (8) corresponds to the surface element of $\mathbb{S}^2$, and its integral over the manifold yields 4π. The pull-back of this integral to $\mathbb{S}^3$ recovers the Hopf mapping degree. In the context of helicity, this topological invariant represents the self- and mutual-linking numbers of a knotted flux tube family [36]. As helicity constitutes the abelian version of the Chern-Simons action, it encodes topological information regarding knots and 3-manifolds [37,38].

2.2 Properties of the spherical Clebsch map

The spherical Clebsch map preserves the structural transparency of the original Clebsch representation while addressing its inability to represent flows with non-zero helicity, and it encodes velocity fields through functions that carry information about the underlying dynamics. A detailed account of the original formulation and its multi-component extensions is given in Appendix A1.

The unit-length constraint $|\boldsymbol{\varsigma}| = 1$ ensures that each $\boldsymbol{\nabla}\boldsymbol{\varsigma}_k$ is perpendicular to the vorticity direction defined in eq. (8), implying

$$\boldsymbol{\omega}_\varsigma \cdot \boldsymbol{\nabla}\boldsymbol{\varsigma}_k = 0, \quad k = 1, 2, 3, \tag{10}$$

such that $\boldsymbol{\omega}_\varsigma$ is tangent to each $\boldsymbol{\varsigma}_k$ level surface. Physically, the velocity field $\boldsymbol{u}_\psi$ in eq. (6) shares the same mathematical structure as the Wu-Yang potential of a non-abelian magnetic monopole [39]. Consequently, its corresponding vorticity field in $\boldsymbol{\omega}_\varsigma$ (8) can be identified as the pull-back of the surface element of the unit sphere $\mathbb{S}^2$. A detailed derivation of eq. (10) can be found Appendix A1. This property is essential for the visualization, interpretation, and computation of vortex structures [4,19,40-43].

Moreover, the spherical Clebsch map provides a gauge-invariant scalar representation for describing different fluid dynamics [44,45], including inviscid flows governed by the Euler equations [46], viscous flows governed by the Navier-Stokes (NS) equations[47], and ISFs [4].

For inviscid flows, the material conservation of spherical vorticity $\boldsymbol{\varsigma}$, as described by Ertel's theorem [48], becomes explicit when the Euler equations are reformulated using the quaternionic ansatz ψ. This formulation captures dissipation-free dynamics while preserving the topological structure of the flow.

For viscous fluid dynamics, the viscosity introduces dissipation, breaking material conservation of the spin and degrading the Clebsch structure. One approach is to introduce a virtual velocity that advects vortex surfaces as material sets [49]. Another approach uses unit-vector formulations to correct the vortex surface field by constructing an effective pressure while modeling incompressible NS dynamics [47].

The ISF dynamics are described by the following constrained Gross-Pitaevskii (GP) equation [50], where pressure enforces incompressibility

$$\frac{\partial\psi}{\partial t} = \mathrm{i}\,\frac{\hbar}{2}\nabla^2\psi - \mathrm{i}\,\frac{1}{\hbar}p\,\psi. \tag{11}$$

The ISF bridges the gap between Euler and NS dynamics by introducing a nonlocal, viscosity-like effect [16] that enables vortex creation, disconnection, splitting, and reconnection without invoking the full viscosity of the NS equations.

3 Quaternionic lifting of spherical Clebsch maps

We formulate a lifting problem: given a smooth spin field on a three-dimensional domain, does there exist a smooth, nor-

malized wave function that enforces incompressibility and reproduces the same vorticity through the Clebsch representation, i.e., the process of the blue arrow in Figure 2? Under a mild compact-support assumption, we prove that such lifts exist and can be chosen periodic; after fixing a natural velocity gauge and a global phase. we obtain uniqueness; a variational principle then characterizes the lift. Specifically, for a smooth $\varsigma : \Omega \to \mathbb{H}_{\mathbb{S}^2}$, we seek $\psi : \Omega \to \mathbb{H}_{\mathbb{S}^3}$ such that $\varsigma = \pi \circ \psi$. We proceed with this formulation under the compact-support hypothesis outlined below.

Problem 1 Let $\Omega \subset \mathbb{R}^3$ be the closed cube of side 2π and let $\varsigma : \Omega \to \mathbb{H}$ satisfy $\mathrm{Re}(\varsigma) = 0$, $|\varsigma| = 1$. Does there exist a smooth periodic $\psi : \Omega \to \mathbb{H}$ such that:

(I) $\|\psi\|^2 = 1$ (2),

(II) $\mathrm{Re}(\nabla^2\overline{\psi}\,\mathrm{i}\,\psi) = 0$ (7),

(III) $\varsigma = \overline{\psi}\,\mathrm{i}\,\psi$ (3),

(IV) the induced velocity $\boldsymbol{u}_\psi = \hbar\,\mathrm{Re}(\nabla\overline{\psi}\,\mathrm{i}\,\psi)$ satisfies (9)?

Is the lift unique?

Proposition 1 Let Ω be a closed topological 3-ball that is a smooth manifold with boundary, and let $\varsigma : \Omega \to \mathbb{H}$ be smooth and satisfy $\mathrm{Re}(\varsigma) = 0$, $|\varsigma| = 1$. Assume there is a smoothly closed topological 3-ball $B \subset \mathrm{int}(\Omega)$ such that $\varsigma|_{\Omega\setminus B} = \varsigma_c$ is constant. Then there exists a smooth map $\psi : \Omega \to \mathbb{H}$ such that (i) ψ satisfies eqs. (2) and (3); and (ii) there is a closed 3-ball B' with $B \subset \mathrm{int}\,B' \subset B' \subset \mathrm{int}(\Omega)$ and $\psi|_{\Omega\setminus B'} = \psi_c$ constant.

Proof Since domain Ω is contractible, a continuous lifting $\hat{\psi} : \Omega \to \mathbb{H}$ exists such that it satisfies both the normalization (2) and the Hopf constraint (3), as shown in Chern et al. [19].

Given that ς is constant outside B, the image $\varsigma|_{\Omega\setminus B} = \varsigma_c$ corresponds to a fixed point under the Hopf map and its preimage $\pi^{-1}(\varsigma_c)$ is isomorphic to $\mathbb{S}^1$. Choose a representative $\psi_c \in \pi^{-1}(\varsigma_c)$, and define a constant map

$$\begin{aligned}\tilde{\psi} : \Omega &\to \pi^{-1}(\varsigma_c),\\ \boldsymbol{x} &\mapsto \psi_c.\end{aligned} \tag{12}$$

Since the space $\mathrm{int}(\Omega) \setminus B$ retracts onto $\mathbb{S}^2$, and all continuous maps from $\mathbb{S}^2$ to $\mathbb{S}^1$ are null-homotopic which implies that all continuous maps from $\mathrm{int}(\Omega) \setminus B$ to $\pi^{-1}(\varsigma_c)$ are null-homotopic, then there exists a homotopy

$$\begin{aligned}H : (\,\mathrm{int}(\Omega) \setminus B) \times [0,1] &\to \pi^{-1}(\varsigma_c),\\ H(\boldsymbol{x}, 0) &= \hat{\psi}(\boldsymbol{x}),\\ H(\boldsymbol{x}, 1) &= \tilde{\psi}(\boldsymbol{x}).\end{aligned} \tag{13}$$

Let B' be a closed topological 3-ball such that $B \subset \mathrm{int}(B') \subset B' \subset \mathrm{int}(\Omega)$. By Urysohns lemma [52], there exists a continuous function $f : \Omega \to [0,1]$ satisfying

$$f(\boldsymbol{x}) = \begin{cases} 0, & \boldsymbol{x} \in B,\\ 1, & \boldsymbol{x} \in \Omega \setminus \mathrm{int}(B'). \end{cases} \tag{14}$$

We now define the interpolated function $\psi : \Omega \to \mathbb{H}$ by

$$\psi(\boldsymbol{x}) = \begin{cases} \hat{\psi}(\boldsymbol{x}), & \boldsymbol{x} \in B,\\ H(\boldsymbol{x}, f(\boldsymbol{x})), & \boldsymbol{x} \in \mathrm{int}(B') \setminus B,\\ \tilde{\psi}(\boldsymbol{x}) = \psi_c, & \boldsymbol{x} \in \Omega \setminus \mathrm{int}(B'). \end{cases} \tag{15}$$

This construction yields a continuous lifting ψ of ς, and smooth approximations can be constructed by standard mollification arguments. Hence, the result extends to the smooth category.

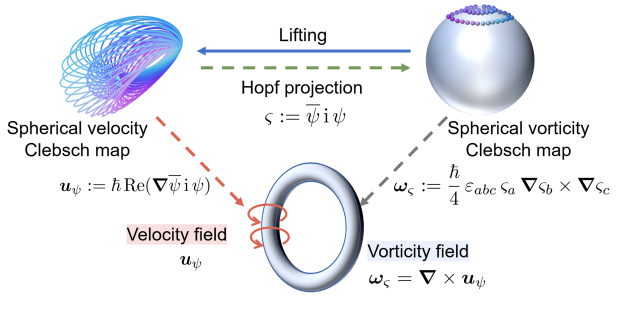

Figure 2 (Color online) Lifting a prescribed spherical vorticity Clebsch map to a spherical velocity Clebsch map. Top: Hopf map $\psi \to \varsigma$ and inverse lifting. Bottom: induced velocity and vorticity fields with $\nabla \times \boldsymbol{u}_\psi = \boldsymbol{\omega}_\varsigma$. The blue arrow marks the optimization that enforces consistency. Here, the visualization of the Hopf fibration is derived following the method introduced by ref. [51].

Proposition 2 Let $\Omega \subset \mathbb{R}^3$ be the closed cube of side 2π, and let $\varsigma : \Omega \to \mathbb{H}$ be smooth and satisfy $\mathrm{Re}(\varsigma) = 0$, $|\varsigma| = 1$. If ς is constant on $\Omega \setminus B$ for some closed 3-ball $B \subset \mathrm{int}(\Omega)$, then there exists a smooth periodic $\psi : \Omega \to \mathbb{H}$ satisfying Conditions (I)-(IV).

Theorem 3 Let ς satisfy $\mathrm{Re}(\varsigma) = 0$, $|\varsigma| = 1$ on Ω. If two periodic solutions ψ_1, ψ_2 satisfy Conditions (I)-(IV) and induce the same velocity $\boldsymbol{u}_\varsigma$, then $\psi_2 = \exp(\mathrm{i}\,\theta_H)\psi_1$ for some constant θ_H.

Theorem 4 Let $\Omega \subset \mathbb{R}^3$ be the closed cube of side 2π, and let $\varsigma : \Omega \to \mathbb{H}$ be smooth, satisfy $\mathrm{Re}(\varsigma) = 0$, $|\varsigma| = 1$, and be constant outside a closed 3-ball $B \subset \mathrm{int}(\Omega)$. Then there exists a unique smooth periodic $\psi : \Omega \to \mathbb{H}$ satisfying Conditions (I)-(IV); its induced velocity $\boldsymbol{u}_\psi$ equals $\boldsymbol{u}_\varsigma$, and it satisfies the gauge constraint $\mathcal{I}(\psi) \in \mathcal{R}_\theta$.

Theorem 5 Let $\Omega \subset \mathbb{R}^3$ be the closed cube of side 2π. Let $\varsigma : \Omega \to \mathbb{H}$ be smooth, satisfy $\mathrm{Re}(\varsigma) = 0$, $|\varsigma| = 1$, and be constant on $\Omega \setminus B$ for some closed ball $B \Subset \Omega$. Assume $\varsigma(\Omega)$ has a nonempty interior point in $\mathbb{H}_{\mathbb{S}^2}$. Consider

$$\begin{cases} \psi = \arg\min\limits_{\phi}\ E_\varsigma(\phi), \\ |\psi| = 1, \qquad \mathrm{Re}(\nabla^2\overline{\psi}\,\mathrm{i}\,\psi) = 0, \qquad \mathcal{I}(\psi) \in \mathcal{R}_\theta, \end{cases} \tag{16}$$

with

$$E_{\varsigma}(\phi)=\frac{1}{2}\left\|\boldsymbol{\nabla}\phi-\frac{\mathrm{i}\,\phi\,\boldsymbol{u}_{\varsigma}}{\hbar}+\frac{\mathrm{i}\,\phi\,\boldsymbol{\nabla}\varsigma}{2}\right\|_2^2, \tag{17}$$

where $\boldsymbol{u}_{\varsigma}$ is the mean-fixed divergence-free velocity satisfying $\boldsymbol{\nabla}\times\boldsymbol{u}_{\varsigma}=\boldsymbol{\omega}_{\varsigma}$. Then the unique minimizer ψ of eqs. (16) and (17) coincides with the unique periodic solution given by Theorem 4 and obeys $\mathcal{I}(\psi)\in\mathcal{R}_{\theta}$.

Firstly, by proving Proposition 1, we point out the existence of the lift without considering the fluid constraints (II) and (IV) in the Problem 1. Then, embedding $\boldsymbol{u}_{\psi}$ and $\boldsymbol{\omega}_{\varsigma}$ in the Hopf fibration, a prescribed spherical vorticity Clebsch map ς should generate a spherical velocity Clebsch map ψ whose induced velocity and vorticity agree with those defined by ς. Equivalently, the lift should also exist under the Constraints (I)-(IV). We ensure this holds by proving Proposition 2. However, existence alone does not fix the lift, since both the hydrodynamic velocity and the global $U(1)$ phase can vary without changing the spin. Theorem 3 identifies these two sources of nonuniqueness. To define the velocity gauge, use the periodic Helmholtz decomposition to obtain a smooth periodic $\tilde{\boldsymbol{u}}_{\varsigma}$ with $\boldsymbol{\nabla}\times\tilde{\boldsymbol{u}}_{\varsigma}=\boldsymbol{\omega}_{\varsigma}$. Its spatial mean may differ from that of $\boldsymbol{u}_{\psi}$, so we set $\boldsymbol{u}_{\varsigma}$ by translating $\tilde{\boldsymbol{u}}_{\varsigma}$ to match means. This fixes the harmonic component on the torus. To fix the global phase, write $\alpha\in\mathbb{H}_{\mathbb{S}^3}$ as $\alpha=\alpha_1+\alpha_2\,\mathrm{j}$ with $\alpha_1,\alpha_2\in\mathbb{C}$, and set

$$\begin{aligned}\mathcal{R}_{\theta}=\Big\{&\alpha=\alpha_1+\alpha_2\,\mathrm{j}\in\mathbb{H}_{\mathbb{S}^3}\ \Big|\\ &\alpha_1,\alpha_2\in\mathbb{C},\ \alpha_{\min(\operatorname{argmax}_{i=1,2}|\alpha_i|)}\in\mathbb{R}^{+}\Big\},\end{aligned} \tag{18}$$

so the component of maximal modulus is positive real, with ties resolved by α_1. Let $\boldsymbol{x}_c$ be the cube center and define the pointwise gauge condition

$$\mathcal{I}:C^{\infty}(\Omega,\mathbb{H}_{\mathbb{S}^3})\to\mathbb{H}_{\mathbb{S}^3},\qquad \mathcal{I}(\psi)=\psi(\boldsymbol{x}_c). \tag{19}$$

With these gauges in place, the lift is completely determined. Finally, we show that the unique periodic lift in Theorem 4 is also the minimizer of a convex quadratic functional subject to the Hopf, normalization, and solenoidal constraints in Theorem 5. Therefore, for a given ς, the spherical velocity Clebsch map ψ can be obtained by finding the minimum of functional (17) through the variational principle. The complete proofs of the Propositions and Theorems about the existence and the uniqueness of the lift is provided in the Supplementary Notes 1B and 2, respectively.

Remark 1 (i) The constraints in eq. (16) are precisely (2) and (7), ensuring incompressibility and Hopf compatibility. (ii) The quadratic form in eq. (17) penalizes the covariant mismatch between $\boldsymbol{\nabla}\phi$ and the connection formed from $\boldsymbol{u}_{\varsigma}$ and $\boldsymbol{\nabla}\varsigma$; if ψ is a solution to the optimization problem in eq. (16), we obtain $\overline{\psi}\,\mathrm{i}\,\psi=\varsigma$ and $\boldsymbol{u}_{\psi}=\boldsymbol{u}_{\varsigma}$. (iii) The velocity gauge fixes the harmonic mean component of $\boldsymbol{u}$ on T^3, while $\mathcal{I}(\psi)\in\mathcal{R}_{\theta}$ fixes the global $U(1)$ phase, which together provide the uniqueness result in Theorem 4.

Remark 2 To uniquely determine the smooth lift ψ, we need both physical constraints and gauge-fixing conditions. The physical constraints are $|\psi|^2=1$, $\mathrm{Re}(\nabla^2\overline{\psi}\,\mathrm{i}\,\psi)=0$, and $\varsigma=\overline{\psi}\,\mathrm{i}\,\psi$. For the gauge conditions, we translate $\tilde{\boldsymbol{u}}_{\varsigma}$ to fix the harmonic mean component, and set the global $U(1)$ phase $\mathcal{I}(\psi)\in\mathcal{R}_{\theta}$. Conversely, the periodic domain and the compact-support hypothesis are technical conditions. Specifically, the compact-support hypothesis ensures the existence of the continuous and smooth lifts in Proposition 1, while the periodic domain ensures that the boundary integrals vanish in eq. (a16).

Figure 2 summarizes the construction. The top edge shows the Hopf mapping from the wave function ψ to the spin field ς and the inverse lifting $\varsigma\mapsto\psi$. The left and right edges display the induced velocity and vorticity, linked by $\boldsymbol{\nabla}\times\boldsymbol{u}_{\psi}=\boldsymbol{\omega}_{\varsigma}$. The blue arrow indicates the optimization that lifts a prescribed spherical vorticity Clebsch map to a consistent spherical velocity Clebsch map.

4 Result

4.1 Spherical vorticity Clebsch maps for knotted vortex tubes with non-zero helicity

We firstly construct explicit spherical vorticity Clebsch maps for vortex tubes of arbitrary topology with variable thickness and uniform twist, following Chui and Moffatt [9], and also refs. [10-15]. Let $C\subset\mathbb{R}^3$ be a smooth closed curve of nonvanishing curvature, parametrized by arclength $s\in[0,L_C]$. Along C, we use the Frenet-Serret (FS) orthonormal frame $\boldsymbol{T},\boldsymbol{N},\boldsymbol{B}$, with $\boldsymbol{T}$ the unit tangent, $\boldsymbol{N}$ the principal normal, and $\boldsymbol{B}=\boldsymbol{T}\times\boldsymbol{N}$ the binormal; $\kappa(s)$ and $\tau(s)$ denote curvature and torsion.

Introduce FS-based tubular coordinates s,ϱ,ϑ via

$$\boldsymbol{x}=\boldsymbol{c}(s)+\varrho\cos\vartheta\,\boldsymbol{N}(s)+\varrho\sin\vartheta\,\boldsymbol{B}(s), \tag{20}$$

and define the tube $\Omega_C=\{\boldsymbol{x}:\min_{0\leqslant s\leqslant L_C}|\boldsymbol{x}-\boldsymbol{c}(s)|<R_v\}$. Choose $R_v>0$ so that s,ϱ are single-valued; the axis is C ($\varrho=0$). Thus, the spherical vorticity Clebsch map reads

$$\varsigma=\varsigma(\Gamma,F,\xi,\sigma), \tag{21}$$

where $\Gamma=1$ is the total toroidal flux, $\xi(s)$ is azimuthal angle twist with local rate, $F(\varrho,s)=2\pi\Gamma\int_0^{\varrho}f(\lambda,s)\,\lambda\,\mathrm{d}\lambda$ is the toroidal flux through radius ϱ at position s with smooth compact profile $f(s)$, and $\sigma(s)$ is the core radius. The specific expression of eq. (21) is provided in the Supplementary Note 3A.

Substituting eq. (21) into the symmetric Clebsch form of ς yields

$$\boldsymbol{\omega}_\varsigma = \Gamma f \varrho \left[(\boldsymbol{\nabla}\varrho - \tfrac{\varrho}{\sigma}\boldsymbol{\nabla}\sigma) \times (\boldsymbol{\nabla}\vartheta - \xi\,\boldsymbol{\nabla}s)\right], \tag{22}$$

consistent with eq. (3.39) of ref. [15]. We illustrate eq. (21) and the induced $\boldsymbol{\omega}_\varsigma$ in a periodic cube of side $L = 2\pi$. Fields are discretized on uniform grids with $N = 512$ for canonical tubes and $N = 1024$ for the turbulent field. In Figure 3(a), we show that the thickness and twist of a canonical vortex tube can be freely controlled by varying $\sigma(s)$ and $\xi(s)$, which enable us to construct vortex tubes of arbitrary topology. For the turbulent field in Figure 3(b)-(d), we generate a skeleton of 50 centerlines via Fourier-series parameterizations with random coefficients and prescribe ς by eq. (21). Isosurfaces of ς_1 reveal tube organization; coloring by $h = \boldsymbol{u}_\varsigma \cdot \boldsymbol{\omega}_\varsigma$ highlights alignment and anti-alignment of $\boldsymbol{u}_\varsigma$ and $\boldsymbol{\omega}_\varsigma$. The spectrum $E(k)$ shows an inertial range close to $k^{-5/3}$ in Figure 3(c), indicating that the construction captures the characteristic cascade phenomenology. The vorticity magnitude squared $|\boldsymbol{\omega}_\varsigma|^2$ is strongly intermittent, as shown in Figure 3(d). A similar structure has also been observed in ref. [53].

4.2 Implementation of quaternionic lifting in the spherical Clebsch map

For a given constructed ς, the lifting ψ can be obtained by solving the optimization problem described in eq. (16). Utilizing the variational method, we take the variation of the functional (17) in the direction ϵ_ϕ of the variable ϕ to obtain the energy variation.

$$\begin{aligned} &E_\varsigma(\phi + \epsilon_\phi) - E_\varsigma(\phi) \\ &= \int_\Omega \left\langle \epsilon_\phi, -\nabla^2\phi + \frac{2\mathrm{i}\boldsymbol{u}_\varsigma \cdot \boldsymbol{\nabla}\phi}{\hbar} - \frac{\mathrm{i}\phi\nabla^2\varsigma}{2} \right. \\ &\left. + \phi\left(\frac{|\boldsymbol{u}_\varsigma|^2}{\hbar^2} + \frac{|\boldsymbol{\nabla}\varsigma|^2}{4}\right)\right\rangle_{\mathbb{R}} \mathrm{d}\,\Omega + O(\|\epsilon_\phi\|^2). \end{aligned} \tag{23}$$

A detailed derivation of this expression can be found in Appendix A2. Thus, the optimal solution of the functional (17) is to solve the following pseudo-time evolution equation

$$\begin{cases} \dfrac{\partial\phi}{\partial\tau} = \nabla^2\phi - \dfrac{2\,\mathrm{i}\,\boldsymbol{u}_\varsigma \cdot \boldsymbol{\nabla}\phi}{\hbar} + \dfrac{\mathrm{i}\,\phi\nabla^2\varsigma}{2} - \phi\left(\dfrac{|\boldsymbol{u}_\varsigma|^2}{\hbar^2} + \dfrac{|\boldsymbol{\nabla}\varsigma|^2}{4}\right), \\ |\phi|^2 = 1, \\ \mathrm{Re}(\nabla^2\overline{\phi}\,\mathrm{i}\,\phi) = 0, \\ \mathcal{I}(\phi) \in \mathcal{R}_\theta. \end{cases} \tag{24}$$

We aim to solve the optimization problem described in (24) by employing a pseudospectral method within the cubic domain $\Omega = [0, 2\pi]^3$. We apply an operator splitting technique, which breaks the problem into smaller subproblems that can

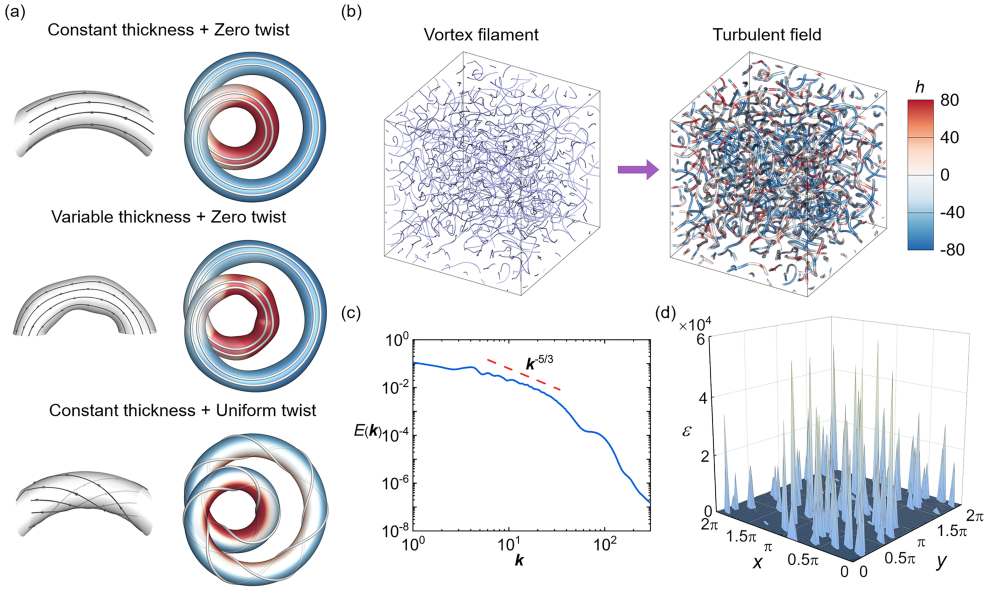

Figure 3 (Color online) Vortex tubes and turbulence from spherical vorticity Clebsch map. (a) Left: schematic vortex surfaces (white) with representative vortex lines (gray). Right: isosurfaces of ς_1 color coded by helicity density $h = \boldsymbol{u}_\varsigma \cdot \boldsymbol{\omega}_\varsigma$. Rows, top to bottom: constant thickness with zero twist; variable thickness with zero twist; constant thickness with uniform twist. (b) Left: a tangle of vortex filaments generated from Fourier-series centerlines with random coefficients. Right: ς_1-isosurfaces colored by h. (c) Energy spectrum $E(k)$ on a 1024^3 grid; the red dashed line indicates Kolmogorov $k^{-5/3}$ scaling. (d) Intermittent vorticity magnitude squared $\varepsilon = |\boldsymbol{\omega}_\varsigma|^2$ in the plane $z = \pi$.

be solved sequentially. The procedure is outlined in the following steps.

Step 1: solving for the velocity-dependent term.

The first step involves solving the two terms of the equation governing the evolution of the wave function ϕ: the velocity field $\boldsymbol{u}_\varsigma$ and the spin field ς. This is done by solving the equation

$$\frac{\partial \phi}{\partial \tau} = -\frac{2\,\mathrm{i}\,\boldsymbol{u}_\varsigma \cdot \boldsymbol{\nabla}\phi}{\hbar} + \frac{\mathrm{i}\,\phi \nabla^2 \varsigma}{2}. \tag{25}$$

Step 2: solving the diffusion equation.

In this step, we solve the diffusion equation

$$\frac{\partial \phi}{\partial \tau} = \nabla^2 \phi, \tag{26}$$

which represents the diffusion of ϕ in the absence of the effects of velocity and spin field.

Step 3: normalization of the wave function.

ϕ is normalized to maintain unit magnitude, as required by the second condition in eq. (24).

Step 4: solenoidal constraint.

We enforce the solenoidal constraint, ensuring that the corresponding velocity field remains incompressible. This is achieved by projecting ϕ onto the space of divergence-free functions. The solenoidal condition is captured by the third equation in eq. (24).

Step 5: phase fixation.

Finally, the phase of ϕ is fixed by projecting it onto the space to ensure that $\mathcal{I}(\phi) \in \mathcal{R}_\theta$ with $\mathcal{R}_\theta$ described in eq. (18). This process is described by the fourth equation in eq. (24).

We evaluated the performance of the algorithm, showing its stability and efficiency. The time complexity is $O(N_t)$ with respect to the number of iterations N_t, and the space complexity is $O(N^3 \log N)$ where N denotes the grid resolution. To demonstrate the robustness of our algorithm with respect to the initial values, we randomized the initial spherical velocity Clebsch map. See Supplement Note 3A for more details. The QLSCM framework is also applied to construct non-torus knot configurations to demonstrate its versatility, as presented in Appendix A3.

A concrete implementation is displayed in Figure 4. For the spherical vorticity Clebsch map ς of a cinquefoil knot, we solve the optimization problem (24) by employing a pseudospectral method within the cubic domain $\Omega = [0, 2\pi]^3$ to lift ς to the spherical velocity Clebsch map ψ. The four components of ψ encode distinct geometric roles. The intersection of the isosurfaces of a and b identifies the vortex axis, while c and d quantify the twist of vortex lines, as further shown in Figures S13 and S14 in Supplementary Note 3B. By applying the lifted spherical velocity Clebsch maps in ISFs, we track the geometric deformation and topological evolution of vortex tubes, revealing the intricate relationship between geometric properties and vortex dynamics, as illustrated in Figure 5. The isosurface of cinquefoil-knot vortex tube representing the vortex core is colored by helicity density to highlight regions where twist accumulates and redistributes. At later times, vortex lines are superimposed on a translucent surface to reveal local alignment and shear structures. Furthermore, vortex tubes with variable thickness promote fragmentation due to localized stress concentrations, while those with uniform twisting stabilize the structure by ensuring a more homogeneous stress distribution, with more details provided in Supplementary Note 3C. Thus, the lifting enables the characterization of the flow's complex features.

5 Conclusion

In this study, we present the first comprehensive mathematical framework for QLSCMs that analytically resolves the solution uniqueness problem using classical formulations.

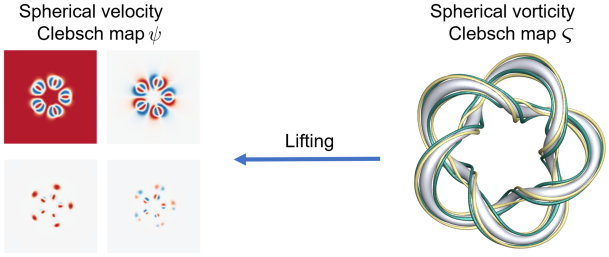

Figure 4 (Color online) A cinquefoil-knot vortex tube from spherical velocity Clebsch map. Left: spatial distribution of a, b, c, and d of ψ in the $z = \pi$ plane through numerical method. Right: isosurfaces of $\varsigma_k, k = 1, 2, 3$ from analytical construction.

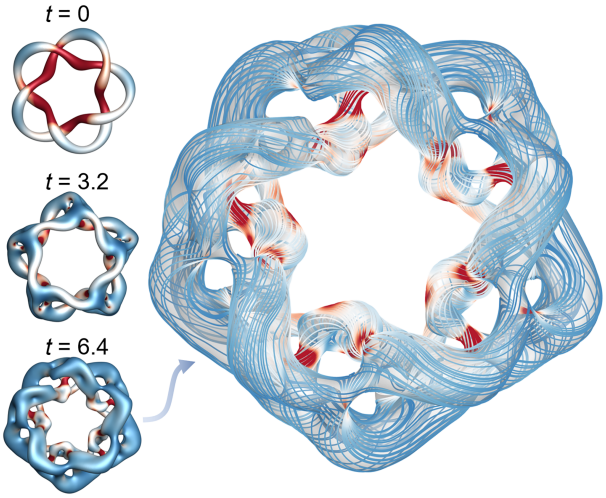

Figure 5 (Color online) ISF evolution of a cinquefoil-knot vortex tube: $\varsigma_1 = -0.4$ isosurfaces colored by helicity density, with a late-time ($t = 6.4$) overlay of vortex lines on a translucent surface.

Building on this foundation, the inverse problem of lifting spherical vorticity Clebsch maps to spherical velocity Clebsch maps reduces to a well-posed extremum problem. Specifically, we construct spherical vorticity Clebsch maps to represent knotted flux tubes of arbitrary topology in a curved cylindrical coordinate system. We then perform the lifting process by solving the extremum problem to obtain the corresponding spherical velocity Clebsch map ψ, which is used as initial conditions to study vortex evolution in ISFs, demonstrating that our approach effectively captures topological changes in vortex tubes.

The QLSCMs framework opens avenues for future research, including its extension to turbulent flows, where vortex interactions and background turbulence are significant. It can also advance understanding of energy transfer and mixing in turbulence, as well as inform flow control strategies by manipulating vortex geometry and topology to manage separation, drag, and mixing in engineering applications. Furthermore, the framework holds potential for quantum computing applications, such as optimizing vortex dynamics simulations or enhancing quantum algorithms for fluid flow modeling.

Remark 3 The compact-support hypothesis ensures that the nontrivial behavior of ς is confined to a contractible region, thereby guaranteeing the existence of the continuous and globally smooth lift. On more general domains, constructing such a lift encounters topological obstructions related to nontrivial $U(1)$ bundles. Spatial periodicity is also necessary for our current mathematical framework, and extending this to non-periodic domains would require a re-evaluation of the propositions regarding solution existence and uniqueness.

This work was supported by the National Key Research and Development Program of China (Grant No. 2023YFB4502600), the National Natural Science Foundation of China (Grant Nos. 12302294, and 12432010), and the Research Fund of the National Key Laboratory of Aerospace Physics in Fluids (Grant No. 2024-APF-KFZD-07).

Conflict of interest The authors declare that they have no conflict of interest.

Supporting Information

The supporting information is available online at http://phys.scichina.com and https://link.springer.com. The supporting materials are published as submitted, without typesetting or editing. The responsibility for scientific accuracy and content remains entirely with the authors.

1 Y. Aharonov, and D. Bohm, Phys. Rev. **115**, 485 (1959).
2 C. Marletto, and V. Vedral, Phys. Rev. Lett. **125**, 040401 (2020).
3 P. L. Saldanha, Phys. Rev. A **109**, 062205 (2024).
4 A. Chern, F. Knöppel, U. Pinkall, P. Schröder, and S. Weißmann, ACM Trans. Graph. **35**, 1 (2016).
5 E. A. Kuznetsov, and A. V. Mikhailov, Phys. Lett. A **77**, 37 (1980).
6 H. Hopf, Math. Ann. **104**, 637 (1931).
7 K. Kucha, Phys. Rev. D **34**, 3031 (1986).
8 G. W. Whitehead, *Elements of Homotopy Theory* (Springer Verlag, New York, 1978).
9 A. Y. K. Chui, and H. K. Moffatt, Proc. R. Soc. London. Ser. A-Math. Phys. Sci. **451**, 609 (1995).
10 H. K. Moffatt, and R. L. Ricca, Proc. R. Soc. London. Ser. A-Math. Phys. Sci. **439**, 411 (1992).
11 F. Maggioni, and R. L. Ricca, Proc. R. Soc. A-Math. Phys. Eng. Sci. **465**, 2761 (2009).
12 S. Xiong, and Y. Yang, Phys. Fluids **31**, 047101 (2019).
13 S. Xiong, and Y. Yang, J. Fluid Mech. **895**, A28 (2020).
14 W. Shen, J. Yao, F. Hussain, and Y. Yang, J. Fluid Mech. **943**, A41 (2022).
15 W. Shen, J. Yao, F. Hussain, and Y. Yang, J. Fluid Mech. **970**, A26 (2023).
16 S. Yang, S. Xiong, Y. Zhang, F. Feng, J. Liu, and B. Zhu, ACM Trans. Graph. **40**, 1 (2021).
17 K. Landsteiner, Y. Liu, and Y. W. Sun, Sci. China-Phys. Mech. Astron. **63**, 250001 (2020).
18 C. Cisowski, J. B. Götte, and S. Franke-Arnold, Rev. Mod. Phys. **94**, 031001 (2022).
19 A. Chern, F. Knöppel, U. Pinkall, and P. Schröder, ACM Trans. Graph. **36**, 1 (2017).
20 S. Ishida, C. Wojtan, and A. Chern, ACM Trans. Graph. **41**, 1 (2022).
21 A. Migdal, Phys. Rep. **1011**, 1 (2023).
22 J. Tang, J. Xiong, A. Minaeian, Y. Jie, and S. Xiong, Sci. China-Phys. Mech. Astron. **68**, 104703 (2025).
23 J. Ashwin, and R. Ganesh, Phys. Rev. Lett. **106**, 135001 (2011).
24 S. Angriman, P. J. Cobelli, M. Bourgoin, S. G. Huisman, R. Volk, and P. D. Mininni, Phys. Rev. Lett. **127**, 254502 (2021).
25 H. Rajamäki, T. Annala, and M. Möttönen, Phys. Rev. Lett. **133**, 236604 (2024).
26 S. Shukla, M. E. Brachet, and R. Pandit, Phys. Rev. D **110**, 083002 (2024).
27 R. Cominotti, A. Berti, A. Farolfi, A. Zenesini, G. Lamporesi, I. Carusotto, A. Recati, and G. Ferrari, Phys. Rev. Lett. **128**, 210401 (2022).
28 Z. Meng, and Y. Yang, Phys. Rev. Res. **5**, 033182 (2023).
29 Z. Meng, and Y. Yang, J. Fluid Mech. **985**, A34 (2024).
30 H. Su, S. Xiong, and Y. Yang, arXiv: 2406.04652.
31 V. E. Zakharov, and E. A. Kuznetsov, Phys.-Usp. **40**, 1087 (1997).
32 E. A. Kuznetsov, Jetp Lett. **76**, 346 (2002).
33 E. A. Kuznetsov, J. Fluid Mech. **600**, 167 (2008).
34 E. A. Kuznetsov, and V. P. Ruban, Phys. Rev. E **61**, 831 (2000).
35 G. T. Horowitz, Commun. Math. Phys. **125**, 417 (1989).
36 H. K. Moffatt, J. Fluid Mech. **35**, 117 (1969).
37 E. Witten, Commun. Math. Phys. **121**, 351 (1989).
38 R. L. Ricca, and M. A. Berger, Phys. Today **49**, 28 (1996).
39 T. T. Wu, and C. N. Yang, Phys. Rev. D **12**, 3845 (1975).
40 P. He, and Y. Yang, Phys. Fluids **28**, 037101 (2016).
41 Y. Yang, and D. I. Pullin, J. Fluid Mech. **661**, 446 (2010).
42 S. Xiong, and Y. Yang, J. Comput. Phys. **339**, 31 (2017).
43 S. Xiong, and Y. Yang, J. Fluid Mech. **874**, 952 (2019).
44 N. Berti, K. Baudin, A. Fusaro, G. Millot, A. Picozzi, and J. Garnier, Phys. Rev. Lett. **129**, 063901 (2022).
45 S. I. Mistakidis, G. Bougas, G. C. Katsimiga, and P. G. Kevrekidis, Phys. Rev. Lett. **134**, 123402 (2025).
46 S. Xiong, Z. Wang, M. Wang, and B. Zhu, ACM Trans. Graph. **41**, 1 (2022).
47 Z. Meng, and Y. Yang, Phys. Rev. Res. **6**, 043130 (2024).
48 H. Ertel, Meteorol. Z. **59**, 271-281 (1942).
49 J. Hao, S. Xiong, and Y. Yang, J. Fluid Mech. **863**, 513 (2019).
50 X. Antoine, W. Bao, and C. Besse, Comput. Phys. Commun. **184**, 2621 (2013).
51 B. O'Sullivan, arXiv: 1601.02569.
52 A. Hatcher, *Algebraic Topology* (Cambridge University Press, Cambridge, 2005).
53 W. Shen, J. Yao, and Y. Yang, Proc. Natl. Acad. Sci. USA **121**,

e2405351121 (2024).
54 A. Clebsch, J. Reine Angew. Math. **56**, 1-10 (1859).
55 Z. Yoshida, J. Math. Phys. **50**, 113101 (2009).
56 Z. Yoshida, and P. J. Morrison, Phys. Rev. Lett. **119**, 244501 (2017).
57 C. Cartes, M. D. Bustamante, and M. E. Brachet, Phys. Fluids **19**, 077101 (2007).
58 C. R. Graham, and F. S. Henyey, Phys. Fluids **12**, 744 (2000).

Appendix

A1 Original Clebsch representation and spherical Clebsch map

The original Clebsch representation, introduced by Clebsch [54], expresses a three-dimensional velocity field in terms of three scalar functions. In its canonical form, the velocity field $\boldsymbol{u}$ is given by

$$\boldsymbol{u} = \boldsymbol{\nabla}\phi + \alpha\boldsymbol{\nabla}\beta, \tag{a1}$$

where (ϕ, α, β) are referred to as Clebsch potentials. The associated vorticity field is then

$$\boldsymbol{\omega} = \boldsymbol{\nabla}\times\boldsymbol{u} = \boldsymbol{\nabla}\alpha\times\boldsymbol{\nabla}\beta. \tag{a2}$$

This formulation implies that vorticity lines lie along the intersections of the level sets of α and β, providing a geometric characterization of vortex structures. In particular, the scalar fields α and β define vortex surfaces via

$$\boldsymbol{\omega}\cdot\boldsymbol{\nabla}\alpha = \boldsymbol{\omega}\cdot\boldsymbol{\nabla}\beta = 0, \tag{a3}$$

indicating that $\boldsymbol{\omega}$ is tangent to both surfaces $\alpha = \text{const}$ and $\beta = \text{const}$. In inviscid flows, these potentials are materially conserved:

$$\frac{D\alpha}{Dt} = \frac{D\beta}{Dt} = 0, \tag{a4}$$

in accordance with Ertel's theorem [48].

However, this single Clebsch representation cannot capture flows with non-zero helicity. The helicity, which quantifies the "twisting", "coiling", "knottedness", or "linkage" of the fluid flow, is defined as:

$$H := \int_\Omega h\,\mathrm{d}\,\Omega = \int_\Omega \boldsymbol{u}\cdot\boldsymbol{\omega}\,\mathrm{d}\,\Omega, \tag{a5}$$

where Ω represents the fluid domain and h denotes the helicity density.

In a simply connected domain with suitable decay or periodic boundary conditions, the helicity (a5) vanishes identically. This follows from the identity

$$\boldsymbol{u}\cdot\boldsymbol{\omega} = \boldsymbol{\nabla}\cdot(\phi\boldsymbol{\nabla}\alpha\times\boldsymbol{\nabla}\beta), \tag{a6}$$

which implies

$$H = \int_\Omega \boldsymbol{\nabla}\cdot(\phi\boldsymbol{\nabla}\alpha\times\boldsymbol{\nabla}\beta)\,\mathrm{d}\,\Omega = \int_{\partial\Omega}\phi(\boldsymbol{\nabla}\alpha\times\boldsymbol{\nabla}\beta)\cdot\boldsymbol{n}\,\mathrm{d}\,S. \tag{a7}$$

where $\boldsymbol{n}$ denotes the outward-pointing unit normal on $\partial\Omega$. If the surface integral vanishes, the helicity is zero.

To overcome this topological limitation, the representation can be extended to include multiple Clebsch pairs [31,55-58]:

$$\boldsymbol{u} = \boldsymbol{\nabla}\phi + \sum_{i=1}^{N_m}\alpha_i\boldsymbol{\nabla}\beta_i. \tag{a8}$$

For $N_m \geqslant 2$, this so-called multi-Clebsch representation can accommodate non-vanishing helicity. The corresponding vorticity is

$$\boldsymbol{\omega} = \sum_{i=1}^{N_m}\boldsymbol{\nabla}\alpha_i\times\boldsymbol{\nabla}\beta_i, \tag{a9}$$

yielding the helicity

$$H = \int_\Omega \boldsymbol{u}\cdot\boldsymbol{\omega}\,\mathrm{d}\,\Omega = \int_\Omega\sum_{i,j}\alpha_i\boldsymbol{\nabla}\beta_i\cdot(\boldsymbol{\nabla}\alpha_j\times\boldsymbol{\nabla}\beta_j)\,\mathrm{d}\,\Omega, \tag{a10}$$

which is generally non-zero. The multi-Clebsch formulation has been applied to describe flows with nontrivial topology, including knotted and linked vortex structures, particularly in plasma and magnetohydrodynamic contexts.

As an alternative, we introduce the spherical Clebsch maps to describe flows with non-zero helicity, and the geometric and Lagrangian coherence of vortex surfaces is always maintained. We first show that the local level surfaces of the scalar fields ς_k for $k = 1, 2, 3$, at regular point $\boldsymbol{x}_0$, i.e., $\boldsymbol{\nabla}\varsigma_k(\boldsymbol{x}_0) \neq \boldsymbol{0}$, for $k = 1, 2, 3$, define local vortex surfaces, in the sense of eq. (a3). Since the coefficients ς_k are smooth and non-vanishing, the gradient vectors $\boldsymbol{\nabla}\varsigma_k$ are linearly dependent at every point, implying the pointwise identity

$$\boldsymbol{\nabla}\varsigma_k\cdot(\boldsymbol{\nabla}\varsigma_{k+1}\times\boldsymbol{\nabla}\varsigma_{k+2}) = 0, \tag{a11}$$

where indices are defined modulo 3. Combining eq. (8) with eq. (a11) yields $\boldsymbol{\omega}_\varsigma\cdot\boldsymbol{\nabla}\varsigma_k = 0, \quad k = 1, 2, 3.$

A2 Variation of the functional

The variation of the functional (17) is evaluated by considering a perturbation in the field variable ϕ in the form of $\phi + \epsilon_\phi$, where ϵ_ϕ represents a small perturbation. The energy variation is expressed as:

$$\begin{aligned} &E_\varsigma(\phi+\epsilon_\phi) - E_\varsigma(\phi) \\ =&\frac{1}{2}\left\|\boldsymbol{\nabla}(\phi+\epsilon_\phi) - \frac{\mathrm{i}(\phi+\epsilon_\phi)\boldsymbol{u}_\varsigma}{\hbar} + \frac{\mathrm{i}(\phi+\epsilon_\phi)\boldsymbol{\nabla}\varsigma}{2}\right\|_2^2 \\ &-\frac{1}{2}\left\|\boldsymbol{\nabla}\phi - \frac{\mathrm{i}\phi\boldsymbol{u}_\varsigma}{\hbar} + \frac{\mathrm{i}\phi\boldsymbol{\nabla}\varsigma}{2}\right\|_2^2. \end{aligned} \tag{a12}$$

Upon expanding the right-hand side of the above expression, we obtain

$$\begin{aligned}&\frac{1}{2}\int_{\Omega}\left(\nabla\phi+\nabla\epsilon_{\phi}-\frac{\mathrm{i}\phi\boldsymbol{u}_{\varsigma}}{\hbar}-\frac{\mathrm{i}\epsilon_{\phi}\boldsymbol{u}_{\varsigma}}{\hbar}+\frac{\mathrm{i}\phi\nabla\varsigma}{2}+\frac{\mathrm{i}\epsilon_{\phi}\nabla\varsigma}{2}\right)\\&\cdot\left(\nabla\overline{\phi}+\nabla\overline{\epsilon_{\phi}}+\frac{\overline{\phi}\mathrm{i}\boldsymbol{u}_{\varsigma}}{\hbar}+\frac{\overline{\epsilon_{\phi}}\mathrm{i}\boldsymbol{u}_{\varsigma}}{\hbar}-\frac{\nabla\overline{\varsigma}\overline{\phi}\mathrm{i}}{2}-\frac{\nabla\overline{\varsigma}\overline{\epsilon_{\phi}}\mathrm{i}}{2}\right)\mathrm{d}\,\Omega\\&-\frac{1}{2}\int_{\Omega}\left(\nabla\phi-\frac{\mathrm{i}\phi\boldsymbol{u}_{\varsigma}}{\hbar}+\frac{\mathrm{i}\phi\nabla\varsigma}{2}\right)\cdot\left(\nabla\overline{\phi}+\frac{\overline{\phi}\mathrm{i}\boldsymbol{u}_{\varsigma}}{\hbar}-\frac{\nabla\overline{\varsigma}\overline{\phi}\mathrm{i}}{2}\right)\mathrm{d}\,\Omega.\end{aligned}\tag{a13}$$

To simplify the expression further, we group similar terms

$$\begin{aligned}&\int_{\Omega}\left\langle\nabla\epsilon_{\phi}-\frac{\mathrm{i}\epsilon_{\phi}\boldsymbol{u}_{\varsigma}}{\hbar}+\frac{\mathrm{i}\epsilon_{\phi}\nabla\varsigma}{2},\nabla\phi-\frac{\mathrm{i}\phi\boldsymbol{u}_{\varsigma}}{\hbar}+\frac{\mathrm{i}\phi\nabla\varsigma}{2}\right\rangle_{\mathbb{R}}\mathrm{d}\,\Omega\\&+O(\|\epsilon_{\phi}\|^{2}).\end{aligned}\tag{a14}$$

This is expanded into four distinct terms

$$\begin{aligned}&\int_{\Omega}\left\langle\nabla\epsilon_{\phi},\nabla\phi-\frac{\mathrm{i}\phi\boldsymbol{u}_{\varsigma}}{\hbar}+\frac{\mathrm{i}\phi\nabla\varsigma}{2}\right\rangle_{\mathbb{R}}\mathrm{d}\,\Omega\\&-\int_{\Omega}\left\langle\frac{\mathrm{i}\epsilon_{\phi}\boldsymbol{u}_{\varsigma}}{\hbar},\nabla\phi-\frac{\mathrm{i}\phi\boldsymbol{u}_{\varsigma}}{\hbar}+\frac{\mathrm{i}\phi\nabla\varsigma}{2}\right\rangle_{\mathbb{R}}\mathrm{d}\,\Omega\\&+\int_{\Omega}\left\langle\frac{\mathrm{i}\epsilon_{\phi}\nabla\varsigma}{2},\nabla\phi-\frac{\mathrm{i}\phi\boldsymbol{u}_{\varsigma}}{\hbar}+\frac{\mathrm{i}\phi\nabla\varsigma}{2}\right\rangle_{\mathbb{R}}\mathrm{d}\,\Omega+O(\|\epsilon_{\phi}\|^{2}).\end{aligned}\tag{a15}$$

(1) Considering the first term of eq. (a15). Using the divergence condition of the velocity field $\boldsymbol{u}_{\varsigma}$, namely $\nabla\cdot\boldsymbol{u}_{\varsigma}=0$, in conjunction with Stokes' theorem, we derive

$$\begin{aligned}&\int_{\Omega}\left\langle\nabla\epsilon_{\phi},\nabla\phi-\frac{\mathrm{i}\phi\boldsymbol{u}_{\varsigma}}{\hbar}+\frac{\mathrm{i}\phi\nabla\varsigma}{2}\right\rangle_{\mathbb{R}}\mathrm{d}\,\Omega\\&+\int_{\Omega}\left\langle\epsilon_{\phi},\nabla^{2}\phi-\frac{\mathrm{i}\boldsymbol{u}_{\varsigma}\cdot\nabla\phi}{\hbar}+\frac{\mathrm{i}\nabla\phi\cdot\nabla\varsigma}{2}+\frac{\mathrm{i}\phi\nabla^{2}\varsigma}{2}\right\rangle_{\mathbb{R}}\mathrm{d}\,\Omega\\&=\int_{\partial\Omega}\left\langle\epsilon_{\phi},(\nabla\phi-\frac{\mathrm{i}\phi\boldsymbol{u}_{\varsigma}}{\hbar}+\frac{\mathrm{i}\phi\nabla\varsigma}{2})\cdot\boldsymbol{n}\right\rangle_{\mathbb{R}}\mathrm{d}\,S\\&=0.\end{aligned}\tag{a16}$$

The last step is obtained due to the periodic boundary condition, where $\boldsymbol{n}$ is a unit vector in the direction of the outer normal of the surface $\partial\Omega$, thus we have

$$\begin{aligned}&\int_{\Omega}\left\langle\nabla\epsilon_{\phi},\nabla\phi-\frac{\mathrm{i}\phi\boldsymbol{u}_{\varsigma}}{\hbar}+\frac{\mathrm{i}\phi\nabla\varsigma}{2}\right\rangle_{\mathbb{R}}\mathrm{d}\,\Omega\\&=\int_{\Omega}\left\langle\epsilon_{\phi},-\nabla^{2}\phi+\frac{\mathrm{i}\boldsymbol{u}_{\varsigma}\cdot\nabla\phi}{\hbar}-\frac{\mathrm{i}\nabla\phi\cdot\nabla\varsigma}{2}-\frac{\mathrm{i}\phi\nabla^{2}\varsigma}{2}\right\rangle_{\mathbb{R}}\mathrm{d}\,\Omega.\end{aligned}\tag{a17}$$

(2) Considering the second term of eq. (a15). Employing the properties of the quaternion norm leads to

$$\begin{aligned}&\left\langle-\frac{\mathrm{i}\epsilon_{\phi}\boldsymbol{u}_{\varsigma}}{\hbar},\nabla\phi-\frac{\mathrm{i}\phi\boldsymbol{u}_{\varsigma}}{\hbar}+\frac{\mathrm{i}\phi\nabla\varsigma}{2}\right\rangle_{\mathbb{R}}\\&=\left\langle\epsilon_{\phi},\frac{\mathrm{i}\boldsymbol{u}_{\varsigma}\cdot\nabla\phi}{\hbar}+\frac{\phi|\boldsymbol{u}_{\varsigma}|^{2}}{\hbar^{2}}-\frac{\phi\boldsymbol{u}_{\varsigma}\cdot\nabla\varsigma}{2\hbar}\right\rangle_{\mathbb{R}},\end{aligned}\tag{a18}$$

furthermore, we obtain

$$\begin{aligned}&\int_{\Omega}\left\langle-\frac{\mathrm{i}\epsilon_{\phi}\boldsymbol{u}_{\varsigma}}{\hbar},\nabla\phi-\frac{\mathrm{i}\phi\boldsymbol{u}_{\varsigma}}{\hbar}+\frac{\mathrm{i}\phi\nabla\varsigma}{2}\right\rangle_{\mathbb{R}}\mathrm{d}\,\Omega\\&=\int_{\Omega}\left\langle\epsilon_{\phi},\frac{\mathrm{i}\boldsymbol{u}_{\varsigma}\cdot\nabla\phi}{\hbar}+\frac{\phi|\boldsymbol{u}_{\varsigma}|^{2}}{\hbar^{2}}-\frac{\phi\boldsymbol{u}_{\varsigma}\cdot\nabla\varsigma}{2\hbar}\right\rangle_{\mathbb{R}}\mathrm{d}\,\Omega.\end{aligned}\tag{a19}$$

(3) Considering the third term of eq. (a15). Adopting a similar operation to the second term of eq. (a15) for the third term, this leads to

$$\begin{aligned}&\left\langle\frac{\mathrm{i}\epsilon_{\phi}\nabla\varsigma}{2},\nabla\phi-\frac{\mathrm{i}\phi\boldsymbol{u}_{\varsigma}}{\hbar}+\frac{\mathrm{i}\phi\nabla\varsigma}{2}\right\rangle_{\mathbb{R}}\\&=\left\langle\epsilon_{\phi},\frac{\mathrm{i}\nabla\phi\cdot\nabla\varsigma}{2}+\frac{\phi\boldsymbol{u}_{\varsigma}\cdot\nabla\varsigma}{2\hbar}+\frac{\phi|\nabla\varsigma|^{2}}{4}\right\rangle_{\mathbb{R}},\end{aligned}\tag{a20}$$

furthermore, we obtain

$$\begin{aligned}&\int_{\Omega}\left\langle\frac{\mathrm{i}\epsilon_{\phi}\nabla\varsigma}{2},\nabla\phi-\frac{\mathrm{i}\phi\boldsymbol{u}_{\varsigma}}{\hbar}+\frac{\mathrm{i}\phi\nabla\varsigma}{2}\right\rangle_{\mathbb{R}}\mathrm{d}\,\Omega\\&=\int_{\Omega}\left\langle\epsilon_{\phi},\frac{\mathrm{i}\nabla\phi\cdot\nabla\varsigma}{2}+\frac{\phi\boldsymbol{u}_{\varsigma}\cdot\nabla\varsigma}{2\hbar}+\frac{\phi|\nabla\varsigma|^{2}}{4}\right\rangle_{\mathbb{R}}\mathrm{d}\,\Omega.\end{aligned}\tag{a21}$$

Substituting eqs. (a17), (a18), and (a21) into eq. (a15) yields the expression in eq. (23).

A3 Non-torus knot configurations in the QLSCM framework

The vorticity field $\boldsymbol{\omega}_{\varsigma}$ and the corresponding velocity field $\boldsymbol{u}_{\psi}$ are constructed for a figure-eight knot and a square knot to illustrate the applicability of the QLSCM framework to diverse topological configurations. As shown in Figure a1, the left column displays the isosurfaces of $|\boldsymbol{\omega}_{\varsigma}|$ color-coded by helicity density with embedded vortex lines, while the right column presents the corresponding slices of the velocity magnitude $|\boldsymbol{u}_{\psi}|$.

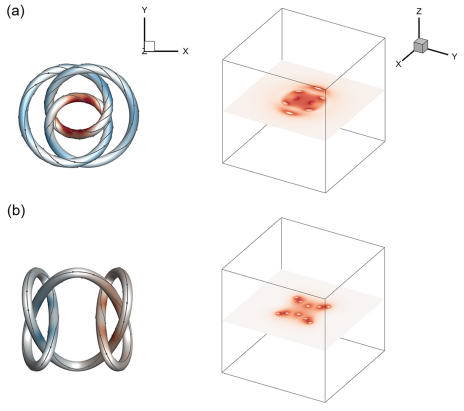

Figure a1 (Color online) Vorticity field $|\boldsymbol{\omega}_{\varsigma}|$ and velocity magnitude $|\boldsymbol{u}_{\psi}|$ for (a) a figure-eight knot and (b) a square knot. Left column: isosurfaces color-coded by helicity density with embedded vortex lines (black). Right column: slices showing the velocity magnitude $|\boldsymbol{u}_{\psi}|$.